ELSEVIER

Contents lists available at ScienceDirect

CIRP Journal of Manufacturing Science and Technology

journal homepage: www.elsevier.com/locate/cirpj





Assessment of cutting force coefficient identification methods and force models for variable pitch and helix bull-nose tools

Joshua Priest^{a,*}, Sabino Ayvar-Soberanis^a, Javier Dominguez-Caballero^a, Peace Onawumi^a, Zekai Murat Kilic^b, David Curtis^a

- a University of Sheffield Advanced Manufacturing Research Centre, Advanced Manufacturing Park, Wallis Way, Catcliffe, Rotherham S60 5TZ, UK
- b Department of Mechanical, Aerospace & Civil Engineering, The University of Manchester, Oxford Road, Manchester M13 9PL, UK

ARTICLE INFO

Keywords:
Cutting force coefficient
Mechanistic
Milling
Rapid testing
Helix angle
Pitch angle
Bull-nose

ABSTRACT

The mechanistic approach is commonly implemented to predict and optimise the cutting forces in milling processes to prevent tool breakages, reduce tool wear, reduce form error, and improve surface quality. To implement this method, the cutting force coefficients (CFCs), that characterise the mechanics of the process, must be calculated. This study compares the accuracy of the predicted cutting forces for variable pitch and helix bull-nose milling tools using a rapid testing (RT) optimisation-based mechanistic CFC identification method that only requires a single angular cut with increasing radial engagement to the traditional mechanistic approach that requires several straight cuts. Along with developing a hybrid technique that combines variation in feed rate and radial engagement. The traditional radial, tangential, and axial (RTA) force model is also compared with the frictional and normal rake face (UV) force model that is independent of the local tool rake and inclination angles which is a necessary for bull nose tools. The RT and the developed hybrid CFC identification method with the UV force model predicted the average F_x , F_y and F_z cutting forces to within 7.1 %, 4.3 %, and 3.8 % error, respectively. These methods were slightly less accurate than the traditional method, however they have significant industrial benefits because they have can be used to identify CFCs with either a single cut, or from any toolpath with chip-load variation, respectively. The RTA force model predicted the average cutting forces similarly to the UV force model, however, the UV force model had lower errors using the rapid RT testing method at the extreme corners of the experimental design space.

1. Introduction

Predicting the cutting forces for milling operations is important to optimise the loading on the tool to prevent breakages and reduce the tool wear, minimise form errors caused by deflections and chatter, reduce the plastic deformation of the machined surface, and optimise the machining-induced residual stresses for better fatigue performance. The cutting forces in milling operations with complex tool paths can be predicted using the traditional mechanistic approach developed by Altintas [1]. This model predicts the radial, tangential, and axial force components from the shearing action which generates the chip and a ploughing action on the machined surface due to the tool edge geometry not being perfectly sharp. The cutting force coefficients (CFCs) capture the complexity of the cutting mechanics for these ploughing and shearing forces individually. These empirical coefficients conveniently collate the effects of the workpiece thermo-mechanical deformation and

the frictional interaction between the tool and the workpiece during cutting. In this form, the macro-geometry of the tool such as the tool rake and relief angles, as well as the cutting-edge geometry are also accounted for within the coefficients.

There are two methods of calculating the CFCs for milling processes, either mechanistically by performing a series of milling tests with constant axial and radial engagement [2] or a series of orthogonal cuts [3] across a range of feed rates. The mechanistic method requires replicating the cutting conditions by using the same tool geometry, workpiece material, cutting speed, and feed rate range being modelled. This method is advantageous because it can account for very complex tool geometry, such as chip breakers and serrated tools, very easily [4]. However, the disadvantage is that the CFCs are only relevant when predicting the cutting forces using the same tool geometry within the range of cutting conditions used in the CFC identification. The mechanistic CFC identification method is commonly implemented by using the

E-mail address: j.priest@amrc.co.uk (J. Priest).

^{*} Corresponding author.

averaged milling forces per rotation of the tool to prevent any impact of the tool run-out [5] and the instability in the forces at the start and end of the chip load [6] on the calculated CFCs.

Kang et al. [7] developed an instantaneous in-process CFC identification method by synchronising the tool-tip positional data from the machine tool with the cutting forces measured using a dynamometer and an optimisation approach to minimise the error in the predicted forces. The predicted CFCs using the in-process identification technique predicted the cutting forces with better accuracy than the traditional averaged CFC method. However, this method was only applied to a simplistic cylindrical end mill with 2 flutes that had consistent geometry. This study also relied upon the predicted response of the model to calculate the initial tool rotational position as it was not measured in-process, which will add complexity for tools with a larger number of flutes that have variable geometry.

Rubeo and Schmitz [5] implemented a similar method to calculate the instantaneous CFCs, but incorporated the tool run-out into the chip thickness and optimised the CFCs using the dynamometer dynamic compensated cutting forces. This study identified higher CFCs at low uncut chip thicknesses using the instantaneous optimisation method compared to the traditional method. This was reportedly due to the feed/rev/tooth approaching the value of the tool edge radius, which causes the effective tool rake angle to become negative compared to the nominal value. However, it was not clarified why there is a larger difference between the CFC identification methods at lower uncut chip thicknesses.

Engin and Altintas [8] developed a generalised mechanistic model using the traditional Altintas [1] force model for solid end milling operations which can be used to model several different types of end mill, such as cylindrical, bull nose, ball end, and tapered barrel tools. Gradišek et al. [2] then modified this model further to consider the effect of the helix angle on the ploughing forces.

Comak et al. [9] modified this model to consider variable pitch and helix tools to optimise the pitch and helix angles for chatter stability, although, the accuracy of the force prediction model was not assessed. Tunç et al. [10] implemented this variable pitch and helix model with a CAD-based geometric engagement calculation method to predict the cutting forces for tools with irregular geometry (such as serrated tools) in 5-axis milling operations. The average forces for a range of tools such as profiling, variable pitch and helix bull nose, and taper ball end milling tools were within 7 % using CFCs calculated using the orthogonal cutting method. However, the stationary time-domain response lacked accuracy when used with the variable pitch and helix bull nose tool.

This general mechanistic model for solid end mills with the averaged mechanistic CFC testing method has been applied to bull nose tools, and some report very good agreement in the resultant predicted cutting forces compared to the experimental response [8,11]. However, others have highlighted that, although good agreement in the average cutting forces is achieved, there are larger discrepancies between the predicted and measured stationary time-domain force response [12,13]. These discrepancies may be a result of the tool run-out not being accurately considered, the accuracy of the CFCs used to predict the shearing and ploughing forces of the tool, dynamic instabilities in the process, or a combination of the above.

Kaymakci et al. [14] developed a generalised model for indexable milling operations that calculated the CFCs for the normal (F_{ν}) and frictional (F_{ν}) forces in the tool rake face. The respective K_{ν} and K_{u} force coefficients (UV) are, unlike the traditional RTA force model, independent of the local cutting-edge inclination and rake angles. Therefore, this method is advantageous for tools with variable helix geometry that have variation up the flute, such as bull nose tools. The additional advantage of this method is that theoretically, assuming the cutting-edge geometry is consistent, they can be mechanistically identified and used with different machining processes. To implement this method, the chip flow angle must be approximated, and the normal rake angle of the tool is required. However, chip flow angle is a complex variable that is

dependent on the local mechanics of cutting and measuring the actual local rake angle on complex tools requires full tool scan data. Stabler's approximation for the chip flow angle is commonly used, as used by Kaymakci et al. [14], which assumes the chip flow angle is equal to the local inclination angle, which is not an accurate assumption [15]. To address this Lorain et al. [16], implemented an experimentally measured value for drilling operations. Kilic et al. [17] further developed the model by Kaymakci et al. [14] to consider the edge coefficients in the oblique RTA coordinate system because these are non-physical parameters in the plane of the rake face. This model also considered the effect of the process vibrations on the chip thickness, predict chatter stability, and added the process damping ploughing force which arises from the cutting process to dampen the vibration energy [18]. This was applied to cylindrical and serrated cylindrical end milling tools, which predicted the averaged cutting forces and the stationary time-domain response well, although, error values were not published. Lorain et al. [16] also implemented a method to consider the uncertainty of the measured force coefficients using this modified force model, however, further research to understand the uncertainty in the resultant predicted forces is necessary.

Liu et al. [19] implemented this modified force model using an in-process CFC identification technique based on the average force method. This was implemented by performing an angular cut with increasing radial depth of cut to increase the chip load, and the CFCs were calculated by a least squares optimisation approach using the averaged cutting forces per revolution of the tool. The CFCs were used to predict the cutting forces in a simplistic cylindrical end-milling operation, which agreed very well with the experiment. This model was also used to demonstrate the increase in ploughing coeffects due to flank wear, which did not significantly impact the shearing coefficients. A potential limitation of this method is that changing the radial engagement varies the chip-load through changing the length of the engagement arc, which reduces the amount of chip-load variation compared to the traditional mechanistic approach that utilises variable feed rates. However, previously, this limitation was not explored and it was not compared to the traditional testing method. Additionally, the method was not applied to more complex tools with variable flute geometry, and, because a cylindrical end mill was used, the study did not take advantage of the benefits of the modified UV force model.

A generalised method using the F_u and F_v (UV) force model for calculating the CFCs for both isotropic and anisotropic materials using an FFT-based approach was developed by Bahram et al. [20]. This method estimated the K_u and K_v shearing and ploughing coefficients using Fourier Series of the CFCs, also enabling the capture of the CFCs with uncut chip thickness, cutting speeds, flank wear. Due to the use of the UV force model, the CFCs calculated from drilling tests were transferable and used to accurately predict the forces in a milling operation. This method was used to simulate a drilling and slot milling operation and compared well to CFCs identified using the orthogonal cutting approach. However, this method was not compared to other mechanistic identification techniques to understand its relative performance and it has not yet been applied to complex variable pitch and helix tool geometries.

Several mechanistic force models and CFC identification testing methods are available to predict the cutting forces in milling operations, however, there is little guidance in the literature on which are the most suitable and how they compare. The purpose of this study is to explore the merits and limitations of the more recently developed angular cutting CFC identification technique and the modified UV force model, by comparing them to the traditional CFC identification method that uses several straight cuts with different feed rates and the RTA force model, respectively. A bull-nose tool with variable pitch and helix angles was selected to leverage the advantages of the UV force model and compare it to the RTA approach. This study highlights the shortcomings of the angular cutting CFC identification technique developed by Liu et al. [19] in terms of its limited chip-load variation, which has not been previously

explored in the literature. To address this limitation, a novel hybrid approach to CFC identification that uses a combination of feed rate and radial engagement variation is proposed. There are also very few studies that assess the performance of the mechanistic modelling approaches for solid end milling tools with variable pitch and helix angles, and the angular cutting CFC identification method has only been previously implemented using a simplistic cylindrical end milling tool.

2. Model development

The differential cutting forces are calculated in the radial dF_r , tangential dF_t , and axial dF_a directions, using the RTA model, shown by the black arrows in Fig. 1a, for each axial differential element (k) with chip width db_k and thickness $h(\varphi_{j,k},\kappa_k)$, shown by the grey area in Fig. 1b, using Eq. 1 [1]. The chip thickness is a function of the local lead angle κ_k and the instantaneous rotation angle $\varphi_{j,k}$, shown in Fig. 1a. $K_{(r,t,a)c}$ represents the chip load coefficients, whilst $K_{(r,t,a)e}$ represents the ploughing coefficients, in the radial, tangential, and axial directions, respectively. Each flute (j) is individually discretised to model variation in the flute geometry. To predict the cutting forces in the tool X,Y,Z coordinate system, these forces must be transformed using the geometric transformation matrix in Eq. 2.

$$dF_r = K_{rc}h(\varphi_{j,k}, \kappa_k)db_k + K_{re}dS_{j,k}$$

$$dF_t = K_{tc}h(\varphi_{j,k}, \kappa_k)db_k + K_{te}dS_{j,k}$$

$$dF_a = K_{ac}h(\varphi_{j,k}, \kappa_k)db_k + K_{ae}dS_{j,k}$$
(1)

$$\begin{pmatrix} dF_{x} \\ dF_{y} \\ dF_{z} \end{pmatrix} = \begin{bmatrix} -\sin\varphi_{j,k}\sin\kappa_{k} & -\cos\varphi_{j,k} & -\sin\varphi_{j,k}\cos\kappa_{k} \\ -\cos\varphi_{j,k}\sin\kappa_{k} & \sin\varphi_{j,k} & -\cos\varphi_{j,k}\cos\kappa_{k} \\ \cos\kappa_{k} & 0 & -\sin\kappa_{k} \end{bmatrix} \begin{pmatrix} dF_{r} \\ dF_{t} \\ dF_{a} \end{pmatrix}$$
 (2)

The instantaneous engagement angle $(\varphi_{j,k})$ is calculated using Eq. 3, which uses the formulation from Budak et al. [9] to consider variable helix (i_j) angles for each flute (j). This has been further adapted in this research to consider variable pitch angles (φ_{p_j}) . The reference rotation angle $\varphi_0(t)$ is the angle of the reference flute in time, as shown in Fig. 1a and the lag angle $(\psi_{j,k})$ is the angle at which the cutting edge trails behind the reference rotation angle at each axial increment up the flute (k).

$$\varphi_{j,k} = \varphi_0(t) + \sum_{n=1}^{j} \varphi_{p_j} - \psi_{j,k}$$
(3)

To model the geometry of the bull nose tool, the formulation for generalised end milling tools, as outlined by Engin and Altintas [8], is used. The instantaneous chip thickness $h(\varphi_{j,k},\kappa_k)$ is calculated using Eq. 4, where f_t is the feed/rev/flute; and $g(\varphi_{j,k})$ is a logic function, as shown in Eq. 5, to determine if the local axial increment is engaged in-cut or not (i.e. within the range of the start and exit angles or not). This takes the value 1 or 0 depending on if the increment is in or ont the cut, respectively. The local start (φ_{start_k}) and exit angles (φ_{exit_k}) are also dependent on the local axial increment and are calculated using the instantaneous radius in Eq. 8. The chip width (db_k) , shown in is calculated using Eq. 6, which is equal to the axial increment dz on the cylindrical section of the bull nose end mill (when $\kappa_k = 90^\circ$). The cutting-edge engagement length $(dS_{j,k})$ is calculated using Eq. 7.

$$h(\varphi_{ik}, \kappa_k) = f_t \sin\varphi_{ik} \sin\kappa_k g(\varphi_{ik})$$
(4)

$$g(\varphi_{j,k}) = \begin{cases} 1, & \varphi_{exit,k} \le \varphi_{j,k} \le \varphi_{start,k} \\ 0, & otherwise \end{cases}$$
 (5)

$$db_k = \frac{dz}{\sin \kappa_k} \tag{6}$$

$$dS_{j,k} = \frac{\mathrm{d}z}{\sin\kappa_k \cos i_{l,k}} \tag{7}$$

The local lead angle (κ_k) , shown in Fig. 1a, lag angle $(\psi_{j,k})$, radius (r_k) , and inclination angle $(i_{j,k})$ are dependent on the region of the tool being discretised, either the arc zone or the cylindrical zone. These zones are identified using the axial increment height (z) and the tool bull-nose radius (R). If z < R then the general formulation for the arc zone is used, else if $z \ge R$ then the general formulation for the cylindrical region is used. The local radius (r_k) , lead angle (κ_k) , lag angle $(\psi_{j,k})$, and inclination angle $(i_{j,k})$, are calculated using Eqs. 8, 9, 10, and 11, respectively. The local inclination angle (i.e. helix angle) in the bull nose region varies from the nominal flute helix angle in the cylindrical section i_{0_j} because this section has a constant lead flute.

$$r_{k} = \begin{cases} \sqrt{R^{2} - (R - z)^{2}} + \left(\frac{D}{2} - R\right), z < R \\ \frac{D}{2}, z \ge R \end{cases}$$

$$(8)$$

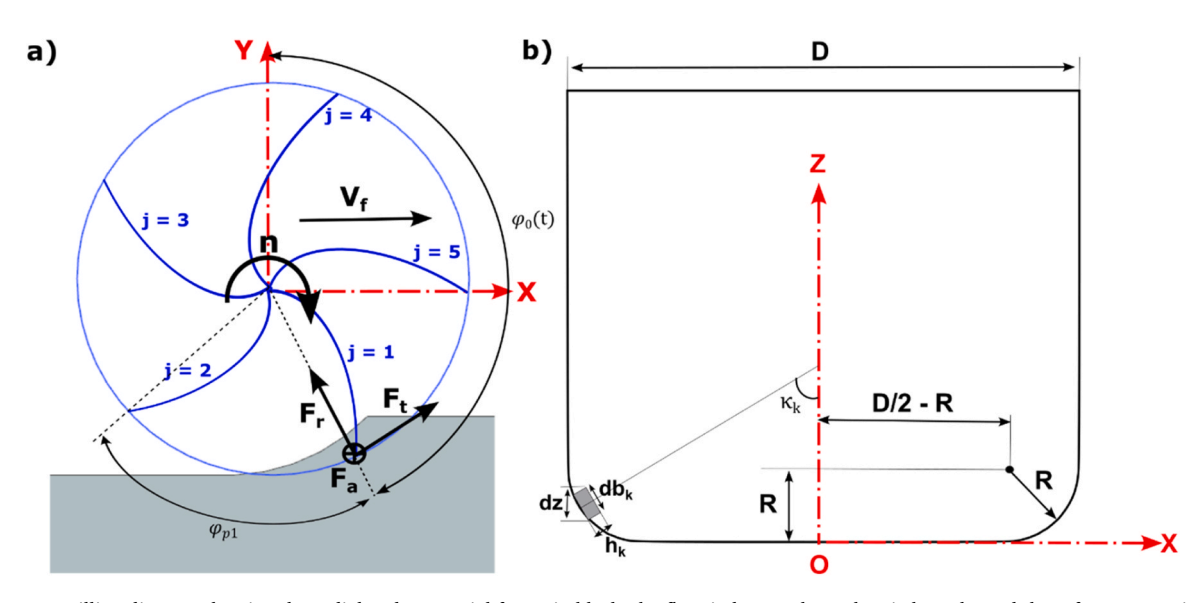


Fig. 1. (a) Down-milling diagram showing the radial and tangential forces in black, the flute index numbers, the pitch angle, and the reference rotation angle. (b) Bull-nose tool geometry showing chip load area highlighted in grey and the arc region geometry.

$$\kappa_{k} = \begin{cases}
\cos^{-1}\left(\frac{R-z}{R}\right), \ z < R \\
\frac{\pi}{2}, \ z \ge R
\end{cases}$$
(9)

$$\psi_{j,k} = \begin{cases} \frac{z \tan i_{j,k}}{R}, \ z < R \\ \frac{z \tan i_{j,k}}{\left(\frac{D}{2}\right)}, \ z \ge R \end{cases} \tag{10}$$

$$i_{j,k} = \begin{cases} \tan^{-1}\left(\left(\frac{r_k - \left(\frac{D}{2} - R\right)}{R}\right) \tan i_{j,0}\right), \ z < R \\ i_{0_j}, \ z \ge R \end{cases}$$
(11)

2.1. Modified force model

The disadvantage of the traditional RTA force model is that the shearing force coefficients cannot be assumed to be constant across all the flutes or independent of the axial increment up the flutes (k) because of the variable helix angles between the flutes and the variable geometry in the bull nose region of the tool [2], [19]. To account for this dependency on the CFCs, the cutting forces are transformed into the frictional forces (dF_u) and normal (dF_v) forces acting in the rake face plane using Eq. 12 as proposed by Kaymakci et al. [14], these forces are shown in Fig. 2. However, in this study, the method proposed by Liu et al. [19] is used which only transforms the shearing coefficients ($K_{uc,vc}$) into the rake face, as shown in Eq. 13. It is not physically correct to have ploughing coefficients in the rake face, therefore, the ploughing coefficients remain in the RTA coordinate system. These $K_{uc,vc}$ coefficients are independent of the geometry of the local axial increment. The angles $\gamma_{n_{j,k}},\lambda_{s_{j,k}}$, and $\eta_{j,k}$ are the local normal rake angle, inclination angle, and chip flow angle, respectively, that potentially vary with the axial increment k.

$$\begin{cases}
dF_r \\
dF_t \\
dF_a
\end{cases} = \begin{bmatrix}
\cos\gamma_{n_{j,k}}\cos\eta_k & -\sin\gamma_{n_{j,k}} \\
\sin\lambda_{s_{j,k}}\sin\eta_k + \cos\lambda_{s_{j,k}}\sin\gamma_{n_{j,k}}\cos\eta_k & \cos\lambda_{s_{j,k}}\cos\gamma_{n_{j,k}} \\
-\cos\lambda_{s_{j,k}}\sin\eta_{j,k} + \sin\lambda_{s_{j,k}}\sin\gamma_{n_{j,k}}\cos\eta_{j,k} & \sin\lambda_{s_{j,k}}\cos\gamma_{n_{j,k}}
\end{bmatrix} \begin{cases}
dF_u \\
dF_v
\end{cases}$$

$$= T_{IU_{j,k}} \begin{cases}
dF_u \\
dF_v
\end{cases}$$
(12)

$$\begin{cases}
K_{rc_{j,k}} \\
K_{tc_{j,k}} \\
K_{ac_{j,k}}
\end{cases} = T_{IU_{j,k}} \begin{Bmatrix} K_{uc} \\
K_{vc} \end{Bmatrix}$$
(13)

The limitations of this method are that the chip flow angle, which is required for the T_{IU} transformation matrix must be approximated, and the local normal rake angle of the flutes is required. In this study, Stabler's rule [21] is used which assumes that the chip flow angle is equal to the local cutting-edge inclination angle, which is also equal to the helix angle for this tool $(\eta_{j,k}=\lambda_{s_{j,k}}=i_{j,k})$. This assumption has limitations because the chip flow angle is also dependent on the cutting speed, uncut chip thickness, tool geometry, the frictional forces in the rake face (i.e. friction angle), and the deformation of the workpiece material in the primary shear zone (i.e. shear angle) [15]. However, for simplicity, these considerations were not implemented in this study. The final parameter required for the $T_{IU_{jk}}$ transformation matrix is the local rake angle which is calculated using Eq. 14.

$$tan\gamma_{n_{j,k}} = tan\gamma_{r_k} cosi_{j,k} \tag{14}$$

2.2. Traditional CFC identification method

To identify the cutting force coefficients using the traditional mechanistic approach, the approach outlined by Gradisek et al. [2] is implemented in this work. The cutting force coefficients using this traditional method require using a series of milling tests with a constant axial (a_p) and radial (a_e) depth of cut using a series of feed rates (f_t) . The variation in the feed rate introduces a variation in maximum chip thickness (h_{ex}) , which the model uses to calculate the CFCs. A linear regression is fitted to the averaged cutting forces as a function of the feed per tooth (f_t) , to calculate the linear slope and intercept terms. It is usually recommended to use at least three different feed rates to improve the robustness of the fitted linear regression [2].

To calculate the shearing coefficients, the shearing force term in the model is integrated between the start (φ_{start}) and exit (φ_{exit}) angles of the cut and equated to the slope of a linear regression that is fitted to averaged cutting forces as a function of the feed per tooth (f_t) . In the same manner, the ploughing coefficients are calculated by equating the intercept of the same regression with the integrated ploughing force term in the model. The equations used to calculate these shear and ploughing coefficients are shown in Eqs. 15 and 16, respectively. N_a and N_f are the number of axial increments and the number of flutes, respectively. The limitation of this implementation of the RTA force model is that it does not consider the variation of the local helix angle and rake angle in the bull-nose region of the tool, which the UV force model considers. It is usually recommended to perform a series of tests with varied axial depths of cut to capture the variations of the CFCs in the bull-nose region [2], however, this is not considered and is a limitation of this study.

$$\left\{ \begin{array}{l} \overline{F}_{x_{S}} \\ \overline{F}_{y_{S}} \\ \overline{F}_{z_{S}} \end{array} \right\} = \sum_{j=1}^{N_{f}} \sum_{k=1}^{N_{a}} \left(\frac{dz}{8\pi} \begin{bmatrix} -\left(2\varphi_{j,k} - \sin 2\varphi_{j,k}\right) & \cos 2\varphi_{j,k} & 0 \\ \cos 2\varphi_{j,k} & 2\varphi_{j,k} - \sin 2\varphi_{j,k} & 0 \\ 0 & 4\cos\varphi_{j,k} \end{bmatrix} \begin{bmatrix} \sin\kappa_{k} & 0 & \cos\kappa_{k} \\ 0 & 1 & 0 \\ -\cos\kappa_{k} & 0 & \sin\kappa_{k} \end{bmatrix} \right) \Big|_{\varphi_{start}}^{\varphi_{extit}} \left\{ \begin{array}{l} K_{rc} \\ K_{tc} \\ K_{ac} \end{array} \right\}$$

$$= \sum_{j=1}^{N_{f}} \sum_{k=1}^{N_{a}} \left(\frac{dz}{8\pi} [A_{k}] [T_{RI_{k}}] \right) \Big|_{\varphi_{start}}^{\varphi_{extit}} \left\{ \begin{array}{l} K_{rc} \\ K_{tc} \\ K_{ac} \end{array} \right\} \tag{15}$$

$$\left\{ \begin{array}{l} \overline{F}_{x_l} \\ \overline{F}_{y_l} \\ \overline{F}_{z_l} \end{array} \right\} = \sum_{j=1}^{N_f} \sum_{k=1}^{N_a} \left(\frac{dS_{k,j}}{2\pi} \begin{bmatrix} \cos\varphi_{j,k} & -\sin\varphi_{j,k} & 0 \\ -\sin\varphi_{j,k} & -\cos\varphi_{j,k} & 0 \\ 0 & 0 & -\varphi_{j,k} \end{bmatrix} \begin{bmatrix} \sin\kappa_k & 0 & \cos\kappa_k \\ 0 & 1 & 0 \\ -\cos\kappa_k & 0 & \sin\kappa_k \end{bmatrix} \right) \Big|_{\varphi_{start}}^{\varphi_{extit}} \left\{ \begin{array}{l} K_{re} \\ K_{te} \\ K_{ae} \end{array} \right\} = \sum_{j=1}^{N_f} \sum_{k=1}^{N_a} \left(\frac{dS_{k,j}}{2\pi} [B_k] [T_{RI_k}] \right) \Big|_{\varphi_{start}}^{\varphi_{extit}} \left\{ \begin{array}{l} K_{re} \\ K_{te} \\ K_{ae} \end{array} \right\} \tag{16}$$

This traditional mechanistic identification method can also be used with the modified force as proposed by Kaymakci et al. [14] by calculating the shearing and ploughing coefficients for the frictional and normal forces in the rake face of the tool using Eqs. 17 and 19, respectively. However, the resultant matrix $[A_k][T_{RI_k}][T_{IU_{jk}}]$ must be solved

the radial depth of cut, or both. This model, as shown in Eq. 20, uses the same formulation as the traditional method, however, the feed per tooth is incorporated back into the shearing force term, and the equations are solved using a least squares optimisation technique as shown in Eq. 18.

$$\begin{cases}
\frac{\overline{F}_{x}}{\overline{F}_{y}} \\
\overline{F}_{z}
\end{cases} = \sum_{j=1}^{N_{f}} \sum_{k=1}^{N_{a}} \left(f_{t} \frac{dz}{8\pi} \begin{bmatrix} -(2\varphi_{jk} - \sin 2\varphi_{jk}) & \cos 2\varphi_{jk} & 0 \\ \cos 2\varphi_{jk} & 2\varphi_{jk} - \sin 2\varphi_{jk} & 0 \\ 0 & 0 & 4\cos\varphi_{jk} \end{bmatrix} \begin{bmatrix} \sin\kappa_{k} & 0 & \cos\kappa_{k} \\ 0 & 1 & 0 \\ -\cos\kappa_{k} & 0 & \sin\kappa_{k} \end{bmatrix} \begin{cases} K_{rc} \\ K_{tc} \\ K_{ac} \end{cases} \right) \\
+ \frac{dS_{k,j}}{2\pi} \begin{bmatrix} \cos\varphi_{j,k} & -\sin\varphi_{j,k} & 0 \\ 0 & -\sin\varphi_{j,k} & 0 \\ 0 & 0 & -\varphi_{j,k} \end{bmatrix} \begin{bmatrix} \sin\kappa_{k} & 0 & \cos\kappa_{k} \\ 0 & 1 & 0 \\ -\cos\kappa_{k} & 0 & \sin\kappa_{k} \end{bmatrix} \begin{cases} K_{rc} \\ K_{te} \\ K_{ae} \end{cases} \right) \begin{bmatrix} \varphi_{exit} \\ K_{te} \\ K_{ae} \end{cases} = \sum_{j=1}^{N_{f}} \sum_{k=1}^{N_{a}} \left(f_{t} \frac{dz}{8\pi} [A_{k}] [T_{Rl_{k}}] \begin{cases} K_{rc} \\ K_{tc} \\ K_{ac} \end{cases} + \frac{dS_{k,j}}{2\pi} [B_{k}] [T_{Rl_{k}}] \begin{cases} K_{rc} \\ K_{te} \\ K_{ae} \end{cases} \right) \begin{bmatrix} \varphi_{exit} \\ K_{te} \\ K_{ae} \end{cases}$$
(20)

using a numerical approach as it is a 3×2 non-symmetrical matrix where only a pseudo inverse of the matrix exists. To solve this problem, the least squares approach, due to its computational efficiency, is used to solve this system of equations and calculate the CFCs that have the best fit to the experimental data.

The averaged cutting forces, in the tool X,Y,Z coordinate system, for each cutting condition (M) are aggregated into a column vector of size $3M \times 1$, the model terms for both the shearing and ploughing forces are aggregated into a vector of size $3M \times 6$, and all six of the CFCs are collated into a column vector 6×1 . The linear system of equations solved for M cutting conditions is shown in Eq. 21.

$$\left\{ \begin{array}{l} \overline{F}_{x_{S}} \\ \overline{F}_{y_{S}} \\ \overline{F}_{z_{S}} \end{array} \right\} = \sum_{j=1}^{N_{f}} \sum_{k=1}^{N_{a}} \left(\frac{dz}{8\pi} \begin{bmatrix} -(2\varphi_{jk} - \sin 2\varphi_{jk}) & \cos 2\varphi_{jk} & 0 \\ \cos 2\varphi_{jk} & 2\varphi_{jk} - \sin 2\varphi_{jk} & 0 \\ 0 & 0 & 4\cos\varphi_{jk} \end{bmatrix} \begin{bmatrix} \sin\kappa_{k} & 0 & \cos\kappa_{k} \\ 0 & 1 & 0 \\ -\cos\kappa_{k} & 0 & \sin\kappa_{k} \end{bmatrix} \right) \begin{bmatrix} T_{IU_{jk}} \end{bmatrix} \right|_{\varphi_{\text{start}}}^{\varphi_{\text{exit}}} = \begin{Bmatrix} K_{uc} \\ K_{vc} \end{Bmatrix}$$

$$= \sum_{j=1}^{N_{f}} \sum_{k=1}^{N_{a}} \left(\frac{dz}{8\pi} [A_{k}] [T_{IU_{jk}}] \right) \Big|_{\varphi_{\text{start}}}^{\varphi_{\text{exit}}} \begin{Bmatrix} K_{uc} \\ K_{vc} \end{Bmatrix}$$

$$(17)$$

if
$$Ax = b$$
, $x = (A^T A)^{-1} A^T b$ (18)

$$\left\{ \begin{array}{l} \overline{F}_{x_{l}} \\ \overline{F}_{y_{l}} \\ \overline{F}_{z_{l}} \end{array} \right\} = \sum_{j=1}^{N_{f}} \sum_{k=1}^{N_{a}} \left(\frac{dS_{k,j}}{2\pi} \begin{bmatrix} \cos\varphi_{j,k} & -\sin\varphi_{j,k} & 0 \\ -\sin\varphi_{j,k} & -\cos\varphi_{j,k} & 0 \\ 0 & 0 & -\varphi_{j,k} \end{bmatrix} \begin{bmatrix} \sin\kappa_{k} & 0 & \cos\kappa_{k} \\ 0 & 1 & 0 \\ -\cos\kappa_{k} & 0 & \sin\kappa_{k} \end{bmatrix} \right) \begin{vmatrix} \varphi_{\text{exit}} \\ K_{\text{re}} \\ K_{ae} \end{vmatrix} = \sum_{j=1}^{N_{f}} \sum_{k=1}^{N_{a}} \left(\frac{dS_{k,j}}{2\pi} [B_{k}] [T_{RI,k}] \right) \begin{vmatrix} \varphi_{\text{exit}} \\ K_{\text{re}} \\ K_{ae} \end{vmatrix}$$
 (19)

$$\left\{ \begin{cases}
\overline{F}_{x} \\
\overline{F}_{y} \\
\overline{F}_{z}
\end{cases} \right\}_{1} \\
\vdots \\
\left\{ \overline{F}_{x} \\
\overline{F}_{y} \\
\overline{F}_{z}
\right\}_{M}
\right\} = \left[\left(\sum_{j=1}^{N_{f}} \sum_{k=1}^{N_{a}} \left(f_{t} \frac{dz}{8\pi} [A_{k}] [T_{RI_{k}}] \right) \Big|_{\varphi_{start}}^{\varphi_{exit}} \right)_{1} \\
\vdots \\
\left\{ \sum_{j=1}^{N_{f}} \sum_{k=1}^{N_{a}} \left(f_{t} \frac{dz}{8\pi} [A_{k}] [T_{RI_{k}}] \right) \Big|_{\varphi_{start}}^{\varphi_{exit}} \right)_{1} \\
\vdots \\
\left\{ \sum_{j=1}^{N_{f}} \sum_{k=1}^{N_{a}} \left(f_{t} \frac{dz}{8\pi} [A_{k}] [T_{RI_{k}}] \right) \Big|_{\varphi_{start}}^{\varphi_{exit}} \right)_{M} \\
\vdots \\
\left\{ \sum_{j=1}^{N_{f}} \sum_{k=1}^{N_{a}} \left(\frac{dS_{j,k}}{2\pi} [B_{k}] [T_{RI_{k}}] \right) \Big|_{\varphi_{start}}^{\varphi_{exit}} \right)_{M} \right\} \left\{ K_{rc} \\
K_{rc} \\
K_{te} \\
K_{ae} \right\}$$
(21)

2.3. Rapid CFC identification method

In contrast to the traditional mechanistic CFC calculation approach, the rapid method takes advantage of the chip load variation caused by either a variation in the feed rate (f_t) (as the traditional method [2]) or variation in

Solving for the radial, tangential, and axial force coefficients directly means that this method does not consider the dependence of the shearing force coefficients with the axial increment (k). To improve this, Eq. 20 has been modified to consider the dependence of the shear force coefficients with the axial increment (k) by substituting in Eq. 13, resulting in Eq. 22.

In this modified method, the force terms are aggregated into the same shape $3M \times 1$ column vector, however, the model terms for the shearing and ploughing forces aggregate into a $3M \times 5$ with a CFC column vector of size 5×1 ; as shown in Eq. 22. This is because the three R, T, A coefficients are reduced to two U. V coefficients in the tool rake face.

3. Experimental methodology

A DMG MORI DMU EVO 40 linear 5-axis CNC machine was used to conduct a series of straight cuts and angular cuts on a square billet of Ti-6Al-4 V Grade 5 using the cutting paraments shown in Table 1; each of these tests was repeated three times. A 16 mm diameter OSG UVX-TI-

$$\begin{cases}
\overline{F}_{x} \\
\overline{F}_{y} \\
\overline{F}_{z}
\end{cases} = \sum_{j=1}^{N_{f}} \sum_{k=1}^{N_{a}} \left(f_{t} \frac{dz}{8\pi} \begin{bmatrix} -(2\varphi_{j,k} - \sin 2\varphi_{j,k}) & \cos 2\varphi_{j,k} & 0 \\ \cos 2\varphi_{j,k} & 2\varphi - \sin 2\varphi_{j,k} & 0 \\ 0 & 0 & 4\cos\varphi_{j,k} \end{bmatrix} \begin{bmatrix} \sin\kappa_{k} & 0 & \cos\kappa_{k} \\ 0 & 1 & 0 \\ -\cos\kappa_{k} & 0 & \sin\kappa_{k} \end{bmatrix} \begin{bmatrix} T_{IU_{j,k}} \end{bmatrix} \begin{Bmatrix} K_{uc} \\ K_{vc} \end{Bmatrix} + \frac{dS_{k,j}}{2\pi} \begin{bmatrix} \cos\varphi_{j,k} & -\sin\varphi_{j,k} & 0 \\ 0 & 0 & -\varphi_{j,k} \end{bmatrix} \begin{bmatrix} \sin\kappa_{k} & 0 & \cos\kappa_{k} \\ 0 & 1 & 0 \\ -\cos\kappa_{k} & 0 & \sin\kappa_{k} \end{bmatrix} \begin{Bmatrix} K_{re} \\ K_{te} \\ K_{ae} \end{Bmatrix} \right) \begin{vmatrix} \varphi_{exit} \\ K_{te} \\ K_{ae} \end{vmatrix} \right) \begin{vmatrix} \varphi_{exit} \\ \varphi_{start} \end{vmatrix} \tag{22}$$

$$\begin{cases}
\left\{ \begin{array}{l} \overline{F}_{x} \\ \overline{F}_{y} \\ \overline{F}_{z} \end{array} \right\}_{1} \\
\vdots \\
\left\{ \begin{array}{l} \overline{F}_{x} \\ \overline{F}_{y} \\ \overline{F}_{z} \end{array} \right\}_{M}
\end{cases} = \left[\left(\begin{array}{l} \sum_{j=1}^{N_{f}} \sum_{k=1}^{N_{a}} \left(f_{t} \frac{dz}{8\pi} [A_{k}] [T_{RI_{k}}] [T_{IU_{jk}}] \right) \Big|_{\varphi_{starr}}^{\varphi_{exit}} \right)_{1} \\
\vdots \\
\left\{ \begin{array}{l} \overline{F}_{x} \\ \overline{F}_{y} \\ \overline{F}_{z} \end{array} \right\}_{M}
\end{cases} = \left[\left(\begin{array}{l} \sum_{j=1}^{N_{f}} \sum_{k=1}^{N_{a}} \left(f_{t} \frac{dz}{8\pi} [A_{k}] [T_{RI_{k}}] [T_{IU_{jk}}] \right) \Big|_{\varphi_{starr}}^{\varphi_{exit}} \right)_{1} \\
\vdots \\
\left\{ \begin{array}{l} \sum_{j=1}^{N_{f}} \sum_{k=1}^{N_{a}} \left(dS_{k,j} [B_{k}] [T_{RI_{k}}] \right) \Big|_{\varphi_{starr}}^{\varphi_{exit}} \right)_{1} \\
\vdots \\
\left\{ \sum_{j=1}^{N_{f}} \sum_{k=1}^{N_{f}} \left(dS_{k,j} [B_{k}] [T_{RI_{k}}] \right) \Big|_{\varphi_{starr}}^{\varphi_{exit}} \right)_{1} \\
\vdots \\
\left\{ \begin{array}{l} K_{uc} \\ K_{vc} \\ K_{re} \\ K_{de} \\ K_{de} \end{array} \right\} \end{cases}$$

$$(23)$$

Both the traditional (Eq. 21) and the modified force models (Eq. 23) are solved using a least squares optimisation procedure to calculate the CFCs in any cutting condition with variation in either the feed rate, the radial depth of cut, or both. This provides an opportunity to calculate the CFCs using data from any tool path that has variation in either the feed rate or radial engagement to provide two or more data sets (*M*). An alternative approach, as proposed by Liu et al. [19], is to use a singular angular cut with increasing (or decreasing) radial depth of cut. The latter experimental approach is adopted in this study to compare the performance of the traditional and modified rapid CFC calculation methods.

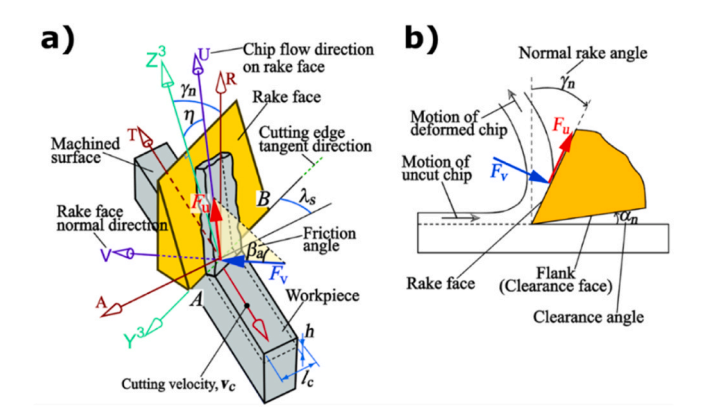


Fig. 2. a) Mechanics of oblique cutting, showing the normal (F_{ν}) and frictional (F_u) forces in the rake face of the tool with respect to the tangential velocity vector (v_0) , the inclination angle (λ_s) , the rake angle (γ_n) , and the chip flow angle (η) . b) Diagram of the forces in the plane normal to the rake face [17].

5FL 5-flute bull nose end mill at a constant 90 m/min (1790 rpm) cutting speed and \sim 8 % concentration Blaser Vasco 7000 emulsion flood coolant was used for all tests. This tool has a 3 mm bull-nose radius, with a constant radial rake, and variable helix and pitch angles. Due to commercial sensitivity, these values cannot be published.

To measure the cutting forces, a Kistler 9255C dynamometer was used which was mounted to the table of the machine tool, with the workpiece mounted on top, as illustrated in Fig. 3. Additionally, a three axis PCB 356A02 accelerometer was mounted to the spindle. The cutting force and accelerometer data was collected using in-house data collection software with a sampling frequency of 51200 Hz. To capture the local tool position, the CNC machine controller data was accessed via Heidenhain LSV/2 protocol at a rate of 333 Hz and transferred via TCP/IP to the PC using the same in-house data collection software. At the end of the data collection, the timestamps from the machine tool controller and the measured force data streams were synchronised by the data monitoring software. It is necessary to capture the actual tool centre position data to accurately calculate the radial engagements and relate these to the measured forces for CFC calculation.

Tests 1-5 are used to calculate the CFCs using the traditional straight cut (TS) approach; therefore, a constant axial and radial depth of cut was used with five feed rates from 0.06 to 0.1 mm/flute/rev. Tests 6-10 were used to calculate the CFCs using the optimisation-based approach with straight cuts (OS) using the same variable feed rate range as in the TS testing (0.06-0.1 mm/flute/rev); however, the radial depth of cut was also varied from 1.6 to 3.2 mm. This OS approach is also benchmarked in this study to compare the CFCs when both the feed rate and radial depth of cut are varied. Test 11 is the rapid angular cut test (RT), where the radial depth of cut was increased from 0.5 mm to 3.2 mm, as shown in Fig. 4. A 0.5 mm starting radial depth of cut was used to ensure that the maximum uncut chip thickness is larger than the

Table 1
Experimental testing parameter sets for the traditional, optimisation, and rapid optimisation approaches to calculate the CFCs. A consistent 90 m/min (1790.19 rpm) cutting speed is used in all tests.

CFC Calculation	Test	Axial Depth of Cut a_p	Feed Rate (mm/flute/	Radial D	epth of Cut a _e (mm)	Maximum uncut chip thickness h_{ex} (mm)			
Method	Number	(mm)	rev)	Start of End of Cut		Start of Cut	End of Cut		
	1		0.06	2.40		0.043			
Traditional	2	10.00	0.07	2.40	Constant throughout	0.050	Constant throughout		
Straight Cuts	3		0.08	2.40	cut	0.057	cut		
(TS)	4		0.09	2.40	cut	0.064			
	5		0.10	2.40		0.071			
Optimisation	6		0.06	1.60		0.036			
	7		0.07	2.00	O	0.046	0		
Straight Cuts	8	10.00	0.08	2.40	Constant throughout	0.057	Constant throughout		
(OS)	9		0.09	2.80	cut	0.068	cut		
	10		0.10	3.20		0.080			
Rapid Test									
Angular Cut (RT)	11	10.00	0.08	0.5	3.2	0.028	0.064		

tool edge radius to form a chip from the start of the test, if it is smaller there is only a ploughing action.

There was a slight lag (\sim 0.3 s) between the machine tool controller and external sensor data streams (i.e. the dynamometer and the spindle

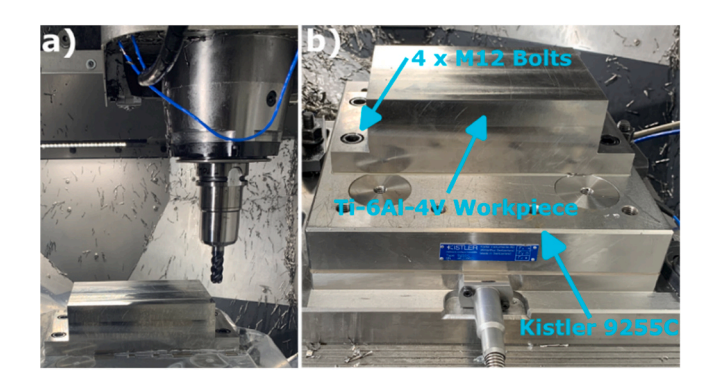


Fig. 3. (a) DMG machine tool, workpiece and milling tool (b) dynamometer mounted on the machine bed and Ti-6Al-4 V workpiece.

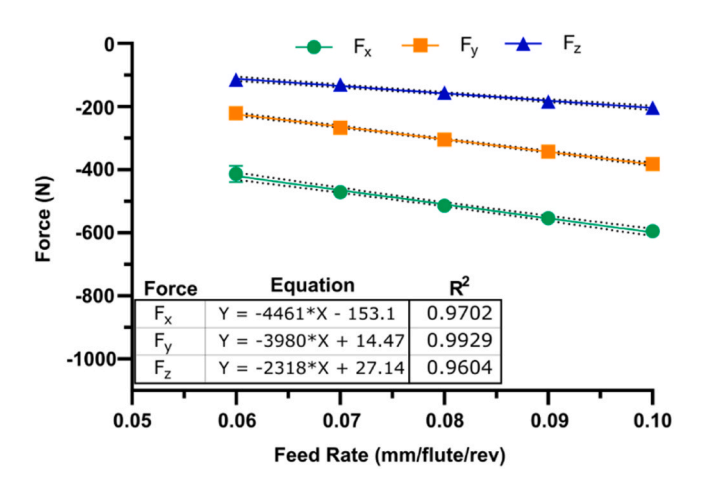


Fig. 5. Averaged F_x (green circles), F_y (orange squares), and F_z (Blue Triangles) cutting forces from the TS test traditional CFC tests, at $a_e=2.4$ mm with $a_p=10$ mm The 95 % confidence interval is represented by the dashed black lines and the standard deviation is shown by the error bars.

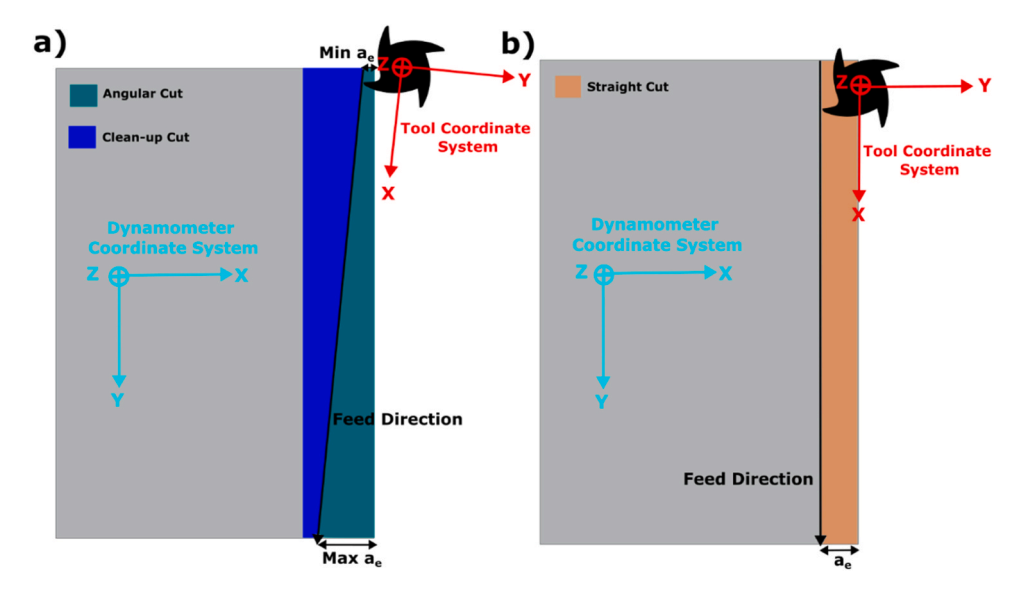


Fig. 4. (a) Angular cut used for the RT testing method with the material removed shown in green and the clean-up cut shown in blue. (b) Straight cut material removed for OS and TS methods shown in orange. The tool and dynamometer coordinate systems are shown in red and blue, respectively.

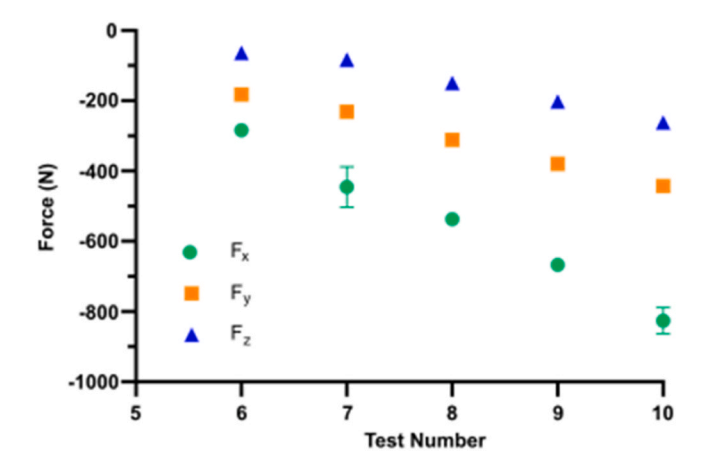


Fig. 6. Averaged cutting forces from the straight cuts calculated in tests 6–10 in the F_x (green circles), F_y (orange squares), and F_z (Blue Triangles) directions. The error bars show the standard deviations across the 3 repeated tests.

accelerometers). However, this was compensated by synchronising the spindle accelerometer response with the machine tool controller spindle positional response when the spindle was turned on.

4. Experimental results and model performance

This section presents the experimentally measured cutting forces in Section 4.1, followed by the calculated CFCs using the different experimental and modelling approaches in Section 4.2, and finally

benchmarks these testing and modelling approaches by comparing the predicted cutting forces to the measured values in Section 4.3.

4.1. Experimental cutting forces

The averaged cutting forces from tests 1–5, with a 10 mm axial depth of cut, are plotted with respect to the feed rate in Fig. 5a and Fig. 5b respectively. These tests had a constant 2.4 mm radial engagement and are plotted in the X,Y,Z coordinate system of the dynamometer for the straight cuts (blue arrows in.

Fig. 4b). The coefficient of variance between the repeated force measurements is less than 2 % across all the cutting conditions, demonstrating the good repeatability of the process. This is shown in Fig. 5 where the error bars represent the standard deviation, however, these are difficult to visualise for some tests as the standard deviations are small. The F_x components (green circles) had the highest magnitude of force, followed by the F_y (orange squares) and F_z (blue triangles) components.

A linear trend was observed for all force components, which is expected because the increase in feed/rev/tooth causes a linear increase in the shearing chip load area. To calculate the CFCs using the traditional mechanistic approach, the linear slope (\overline{F}_S) and intercept (\overline{F}_I) of these trends must be calculated. To do this, a linear regression was fitted to each force component which resulted in a good fit because the R^2 values (shown in Fig. 5) are all greater than 0.96, and the P-values for all of the slopes and intercept coefficients are less than 0.0001. The latter value demonstrates the statistical significance of the trends. The R^2 values and coefficients for these linear regressions are shown in the tables beneath the graphs.

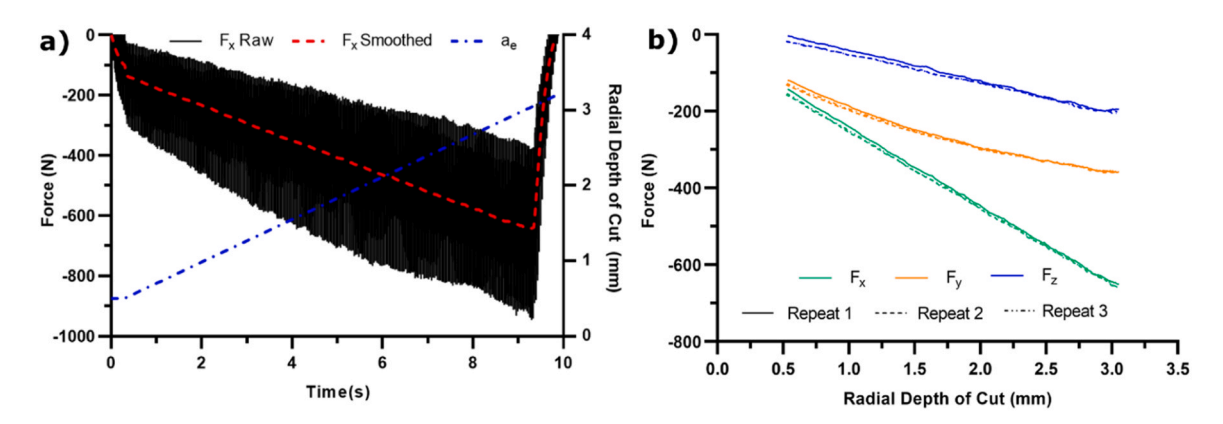


Fig. 7. (a) Example of the raw (black line) and smoothed (dashed red line) F_x force response plotted with the radial depth of cut (blue dashed line). (b) F_x (green lines), F_y , (orange lines) and F_z (blue lines) cutting forces with respect to the instantaneous radial depth of cut, for all three repeats.

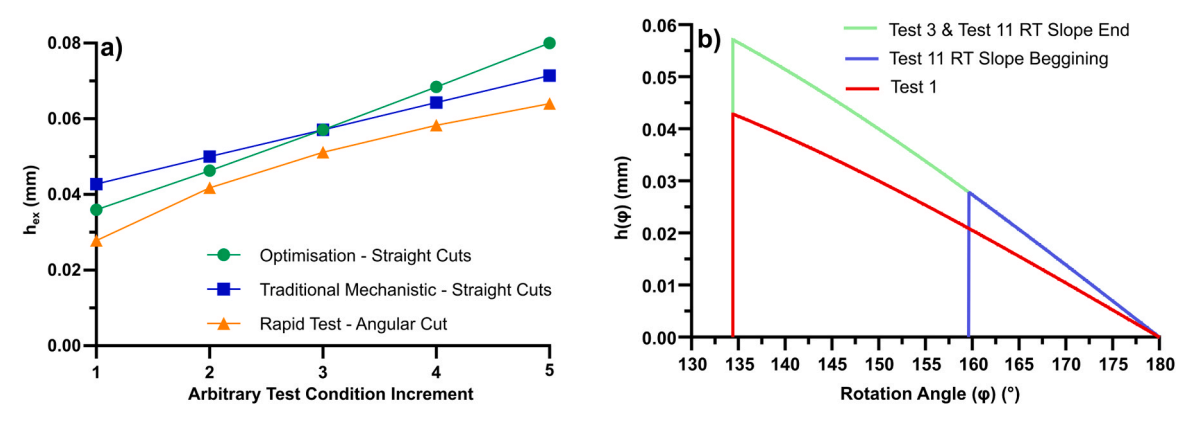


Fig. 8. (a) Average uncut chip thickness at entry angle $h(\varphi_{start})$ for the OS (green circles), TS (blue squares), and the RT optimisation angular cut (orange triangles) methods. (b) Average uncut chip thickness $h(\varphi)$ with rotation angle (φ) for test 3 and test 11 at the end of the slope (green line), test 11 at the beginning of the slope (blue line), and test 1 (red line).

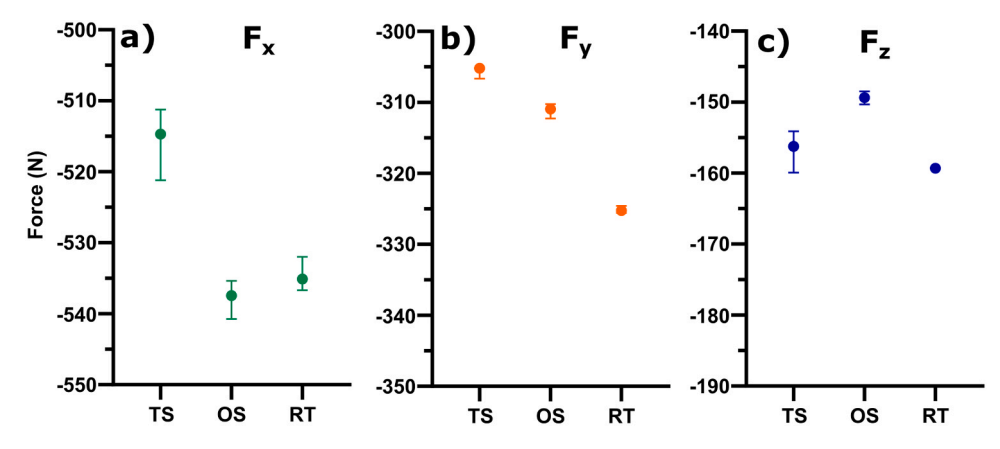


Fig. 9. Comparison of the mean values of the three repeated tests using TS, OS, and RT testing methods at the same chip load condition ($a_e = 2.4$ mm, ft = 0.08, $a_p = 10$ mm hex = 0.057 mm) with respect to the (a) F_x , (b) F_y , and (c) F_z force coefficients. Error bars represent the range of the three repeated measurements.

The averaged cutting forces from tests 6–10, which had a constant (10 mm) axial engagement with increasing radial engagement from 1.6 – 3.2 mm and feed rate from 0.06 – 0.1 mm/flute/rev, are shown in Fig. 6. The magnitude of the F_x (green circles), F_y (orange squares), and F_z (blue triangles) force components increased as the feed rate and radial engagement increased, which is to be expected as both the radial engagement and feed rate increase the shearing chip load area. The coefficient of variance values for all the repeated measurements were all less than 3 %, apart from the F_x components in test number 7 and 10 which had variance up to 11 %, highlighted by the green standard deviation error bars in Fig. 6. This shows that the data had good repeatability, however, the F_x component data was less repeatable than it was in tests 1–5, which had a constant radial engagement.

The force responses of the angular cuts are smoothed with a moving mean that has a window size equal to 1 revolution of the tool. This is illustrated in Fig. 7a, whereby the raw F_x force is shown by the black line and the smoothed force is shown by the dashed red line, the correlated radial depth of cut (a_e) that is calculated based on the machine tool positional data is shown by the dashed blue line. These smoothed forces, in the F_x , F_y , and F_z , directions are shown in Fig. 7b plotted with respect to the radial depth of cut for each of the three repeated tests, which have a linear relationship for each force component. The F_y force component deviated from this linear relationship after approximately $a_e = 2mm$, whereas the F_x force component did not deviate from this linear relationship, and the F_z force component only deviated very slightly towards the end of the cut at $a_e = 3.1mm$.

It is important to highlight that the maximum chip loads (h_{ex}) on the

cylindrical part of the tool, calculated using Eq. 23, differ between the testing methods, as highlighted in Fig. 8a. In this figure, for the TS tests the increment represents tests 1–5, for OS the increment represents tests 6-10, and for the RT tests, five arbitrary increments in the radial depth of cut are plotted. This is because the chip load is dependent on both the feed rate (f_t) and the radial depth of cut (a_e) , therefore, there is an interaction effect between the two parameters. This is why, even though the same range of feed rates that were used in traditional mechanistic cuts (blue squares) and optimisation cuts (green circles), the maximum chip load is different because the radial depth of cut was also varied. The optimisation straight cuts had a lower chip load in the first two tests, then a higher chip load in the last two tests, with an overlap at the centre point test. Additionally, the radial depth of cut has a non-linear relationship with the maximum chip load, therefore, the increase in the chip load is non-linear as shown by the orange triangles. The angular cut also had a lower chip load than the traditional mechanistic and optimisation straight cuts tests due to this interaction effect, even though the range of the radial depth of cut was consistent with the other tests and the feed rate (0.08 mm/flute/rev) was at the centre point. However, regardless of this, the chip load must be incrementally increased to calculate the CFCs, which is satisfied by all three testing methods.

$$h_{ex} = f_t \sin\left(\pi - \cos^{-1}\left(\frac{\frac{D}{2} - a_e}{\frac{D}{2}}\right)\right)$$
 (23)

Fig. 8b also demonstrates a key difference in the chip loading

Table 2Cutting force coefficients calculated using the RTA force model. The percentages in green represent the difference compared to the traditional straight cuts testing method. The units for the shearing (K_c) and ploughing (K_e) coefficients are MPa and N/mm, respectively.

CFC	Traditional	Optimisation Straight Cuts (OS)		Optimisation Rapid Angular Cut (RT)								
(RTA)	Straight Cuts (TS)			Repeat 1		Repeat 2		Repeat 3		Repeat 3 (PSO)		
Krc	786.7	604.0	-23%	341.2	-57%	269.8	-66%	327.9	-58%	907.0	15%	
K_{tc}	2580.6	2259.3	-12%	1299.7	-50%	1125.9	-56%	1200.1	-53%	2059.9	-20%	
K_{ac}	1162.3	1313.8	13%	1834.4	58%	1689.8	45%	1724.1	48%	1682.9	45%	
K_{re}	18.9	26.9	42%	34.1	80%	36.5	93%	34.9	84%	20.0	6%	
K_{te}	5.4	13.0	143%	34.1	536%	38.1	611%	36.5	580%	20.0	273%	
K_{ae}	-0.4	-4.7	1112%	-13.9	3512%	-10.0	2497%	-10.9	2723%	-11.1	2768%	
RMSE (N):		19.2		2.3		2.0	•	1.6		8.20	•	

Table 3
CFCs calculated using the UV force model. The percentages in green represent the difference compared to the TS method. The shearing (K_c) and ploughing (K_e) coefficient units are MPa and N/mm, respectively.

CFC	Traditional	Optimisation Straight Cuts (OS)		Optimisation Rapid Angular Cut (RT)								
(UV)	Straight Cuts (TS)			Repeat 1		Repeat 2		Repeat 3		Repeat 3 (PSO)		
Kuc	1202.9	853.1	-44%	33.4	-97%	34.9	-103%	26.9	-98%	1218.7	1%	
K_{vc}	2693.1	2563.3	-5%	2190.9	-19%	1962.9	-27%	2042.5	-24%	2150.5	-20%	
K_{re}	18.9	28.0	1%	41.0	117%	43.0	127%	41.6	120%	20.0	6%	
K_{te}	5.4	11.6	33%	25.3	371%	29.9	458%	28.0	422%	17.5	225%	
K_{ae}	-0.4	-3.5	-58%	-4.9	1170%	-1.6	320%	-2.2	477%	7.3	-1995%	
RMSE (N):		19.4		6.3		5.8		5.9		11.3		

between the RT and TS CFC identification methods. As shown by comparing the green and blue lines, the RT method varies the chip load by changing the start angle (for down-milling) of the flutes which results in gradually increasing the length of the engagement arc. This means that beyond $\varphi_{j,k} = \sim 159^\circ$, the additional chip loading information extracted from the RT testing method at the end of the sloped cut is the same information that was extracted at the beginning. However, using the TS method, more information is captured about the process because the entire range of uncut chip thickness across the engagement arc varies. This is demonstrated by comparing the chip loading for test 3 at a 0.08 mm/flute/rev feed rate (also represented by green line) with the test 1 (red line) that had a lower 0.06 mm/flute/rev feed rate. The uncut chip thicknesses plotted are the average across all flutes because the variable pitch angle between the flutes results in varied chip loads across them

Tests 3 and 8, using the TS and OS testing methods, respectively, had consistent cutting conditions, which is also consistent with the RT testing method at a radial depth of cut of 2.4 mm. Fig. 9a, b, and c compare the mean cutting forces for each testing method at this condition across the three repeated tests, for the F_x , F_y and F_z force components, respectively. The F_z forces (Fig. 9c) were within a range of \sim 12 N, however, the F_x (Fig. 9a) and F_y (Fig. 9b) forces had slightly larger variation, within the range of \sim 21 N and \sim 30 N, respectively. A one-way ANOVA was performed, which highlighted that the mean values between the testing methods are statistically not equal because the data has p-values of less than 0.002, so the null hypothesis that the mean values are equal is rejected. However, the coefficient of variance is within \sim 3 % across the three repeats for each testing method.

4.2. Cutting force coefficients (CFCs)

The CFCs calculated using the RTA force model using each of the testing methods (TS, OS, RT) at a 10 mm axial depth of cut are shown in Table 2. To ensure consistency between the range of radial depths of cut used in the OS straight cuts tests, the CFCs for the rapid RT tests were calculated using the average force response from 1.6 to 3.2 mm radial depth of cut. The baseline set of CFCs is calculated using the traditional straight-cuts method (TS) with constant axial and radial engagements, and the percentage differences highlighted in the green cells are the deviation of each method from this baseline. Using the RT method, three sets of CFCs were generated because the test was repeated three times.

There is up to a 23 % difference between the shearing coefficients when comparing the TS and OS testing methods. The largest difference in the K_{rc} coefficient. There is an even larger percentage difference between the ploughing coefficients, although, this is because the values are small; the actual nominal differences are within \sim 8 N/mm. Further comparisons between the shearing coefficients will be discussed in percentage terms, however, comparisons of the ploughing coefficients

will be made in terms of the absolute values because the values are small. The rapid RT testing method resulted in CFCs with the largest difference from the benchmark traditional TS method, with differences between the shearing and ploughing coefficients of up to 58 % and 25 N/mm, respectively. To minimise this difference, the particle swarm metaheuristic optimisation (PSO) technique with upper and lower bounds between -20 to 20 N/mm for the ploughing coefficients was used with the data from Repeat 3. This range was selected using the precalculated result using the TS method to ensure that the method does not impose non-physical constraints and to prevent the optimal solution from being on the boundary of the search space. Limiting the ploughing coefficients reduced the difference in the K_{rc} and K_{tc} shearing coefficients to within 20 % of the TS value. However, the K_{ac} remained similar to that calculated using the least squares method, and it resulted in a higher global root-mean-squared-error (RMSE) between the predicted and experimental forces. Additionally, although the rapid RT testing method resulted in larger deviations in the CFCs from the benchmark traditional TS method than the OS method, the rapid RT testing method has lower global RMSE values. This is because a reduction in the shearing coefficients is accompanied by an increase in the ploughing coefficients, apart from in K_{ac} , which potentially balances out the force equation.

The same comparisons between the testing methods are made for the UV force model in Table 3. The deviation of the CFCs using OS testing methods from the traditional TS method is larger using the UV force model compared to the RTA model, with up to 44 % and 10 N/mm difference for the shearing and ploughing coefficients, respectively. The differences in the CFCs calculated using the RT testing method are even larger, however, the RMSE values using the RT method are lower than those using the OS method. This is consistent with the trends observed using the RTA force model, however, the global RSME values using the UV force model are larger than the corresponding values using the RTA force model.

4.3. Predicted cutting forces and model validation

The predicted stationary time-domain responses at the centre point (test 3) cutting condition using the various models are compared to the experimental response in Fig. 10a, b, and c for the F_x , F_y and F_z force components, respectively. The TS-RTA (orange line), OS-RTA (red line), RT-RTA (green line) testing methods using the RTA force model and the TS-UV (blue line), OS-UV (black line), and RT-UV (light blue line) using the UV force model are compared to the experimental response (black dashed line). All the models perform similarly at this cutting condition with the largest deviation between 45–90° of tool rotation where the F_x and F_y force components are underpredicted. The tool rotational angle, with respect to the chosen reference flute, was not measured at the point of first engagement; therefore, the force responses have been manually

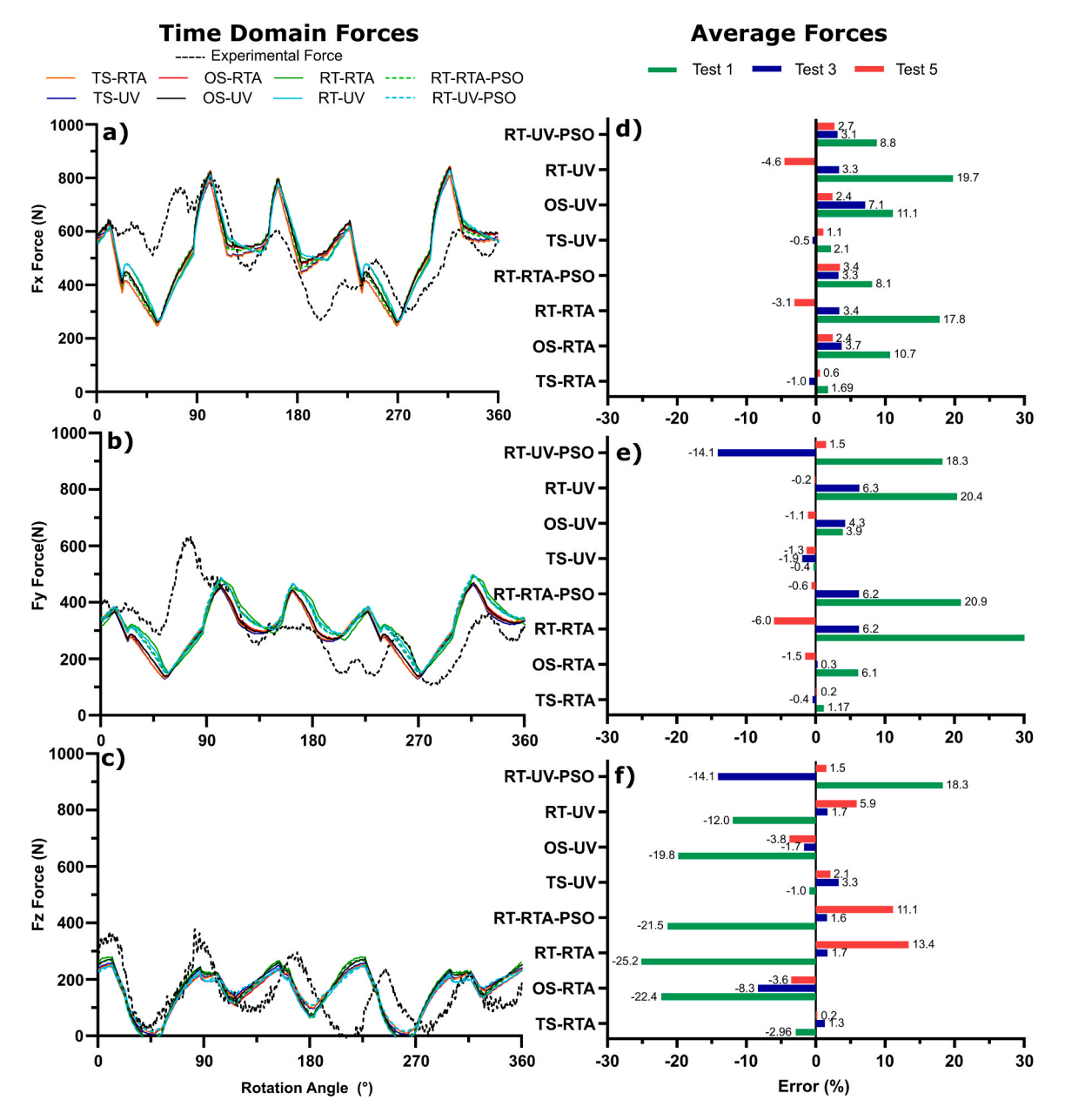


Fig. 10. Comparison of the experimental (black dashed lines – Test 1) with the predicted stationary time-domain responses by the TS-RTA (orange line), OS-RTA (red line), RT-RTA (green line), TS-UV (blue line), OS-UV (black line), and RT-UV (pale blue line) for the (a) F_x , (b) F_y , and (c) F_z force components at test 3 cutting conditions. The average errors between the predicted and experimental cutting forces for the (d) F_x , (e) F_y , and (f) F_z components for test 1 (green bar), test 3 (orange bar), test 5 (red bar), and test 12 (blue bar) conditions.

aligned in a way that minimises the error. Due to the complexity of the tool and the resultant force response with multiple flutes engaged simultaneously, this alignment may have inaccuracies.

The errors in the predicted average cutting forces compared to the experimentally measured values for F_x , F_y and F_z force components are shown for all models in Fig. 10d, e, and f, respectively. The errors at test 1 (green bars), test 3 (orange bars), and test 5 (red bars) were chosen for comparison as they represent the full range of feed rates (0.06-0.1 mm/flute/rev) used to identify the CFCs, with a 2.4 mm radial depth of cut.

Comparing the average forces using the RTA force model, the TS-RTA model has the lowest error which predicted all the force components to be within 3 % of the experiment. The OS-RTA model was the next most accurate model using the RTA force model, predicting the F_x , F_y and F_z forces within 10.7 %, 6.1 %, and 22.4 % error, respectively. Followed by the rapid testing RT-RTA model predicting the cutting

forces to within 17.79 %, 30.27 %, and 25.21 % error, respectively.

The UV force model predicted the average cutting forces consistently with the RTA force model, and the same trends with respect to the testing methods was observed between the different force models. The traditional TS-UV model had the lowest errors using the UV force model, predicting all the force components to be within 3.3 % of the experiment. Followed by the OS-UV model which predicted the F_x , F_y and F_z forces to within 11.1 %, 4.25 %, and 19.84 % error, and lastly the rapid RT-UV model which predicted the average cutting forces, with slightly more error, to within 19.7 %, 20.4 %, and 12 %, respectively.

The largest errors across all these models are at the test 1 cutting condition (green bars), which had the lowest feed rate (0.06 mm/flute/ rev) and the largest variance in the experimental data. At the other cutting conditions tested, the OS and rapid RT testing methods performed much better. Neglecting test 1, the OS-RTA model predicted the F_x , F_y and F_z , to within 3.7 %, 1.5 %, and 8.3 % error, and the rapid RT-

RTA model predicted them to within 3.4 %, 6.2 %, and 13.4 % error, respectively. The models using the UV force model also performed much better when neglecting test 1, the OS-UV model predicted the F_x , F_y and F_z force components to be within 7.1 %, 4.3 %, and 3.8 % of the experiment, respectively, and the rapid RT-UV model predicted them to be within 4.6 %, 6.35 %, and 5.9 % of the experiment, respectively. These errors are in-line with those achieved using the RTA force model.

Comparing the predicted forces at the test 3 condition, which is the only chip load condition that was consistent across all three testing methods, the OS and rapid RT testing methods are in better agreement with the traditional TS method. The OS-RTA and RT-RTA models predicted the average F_x , F_y and F_z cutting forces to within 3.7 %, 0.3 % and 8.3 %, and 3.4 %, 6.2 %, and 1.7 %, respectively. The OS-UV and RT-UV models, using the UV force model, also performed better, predicting the average F_x , F_y and F_z cutting forces to within 7.1 %, 4.3 %, and 1.7 %, and 3.31 %, 6.32 %, and 1.7 %, respectively. Overall, the UV and RTA force models predicted the average cutting forces consistently at this cutting condition. However, at test 1 and test 5 cutting conditions, which are at the lowest and highest feed rates, respectively, the rapid RT method using the UV force model (RT-UV) predicted the average F_{v} and F_z cutting forces much better, by up to 13 % in test 1 % and 7 % in test 5, whilst the F_x cutting forces were consistent. At test 1 and 5 cutting conditions, the rapid RT-RTA model benefited from the particle swarm optimisation (RT-RTA-PSO model) that bounded the ploughing coefficients, which improved the predicted average forces by up to 10 %, bringing the forces in line with the RT-UV model at these conditions. However, the RT-UV-PSO model did not have any significant improvement over the RT-UV model.

5. Discussion

During the experimental testing, good repeatability was achieved with coefficients of variance of less than 3 % on average. The coefficient of variance is the highest at test 1, which was between 4.4 % and 9.4 % for all the force components. This is a potential factor causing the increased error in the predicted cutting forces by all the models at this cutting condition.

However, good consistency was achieved between the measured cutting forces using the three (TS, OS, and rapid RT) testing methods, as compared in Fig. 9. This comparison was made at a radial depth of cut, feed rate, and axial depth of cut of 2.4 mm, 0.08 mm/flute/rev, and 10 mm, respectively, as this is the only overlap in the cutting parameters between the testing methods. This demonstrates that the synchronisation of the machine tool positional data used to calculate the radial depth of cut in the angular rapid (RT) tests is reliable, as the TS and OS straight-cut tests did not rely on the machine tool positional data. This consistency also demonstrates that, even though all the cuts were performed using the same tool, the effect of tool wear was negligible and did not impact the cutting forces.

The three testing methods produced different ranges of chip load across the different methods used to calculate the CFCs, as demonstrated in Fig. 8. This is one of the contributing factors to the differences between the calculated CFCs using the traditional TS and the OS and RT testing methods. The chip load increases during the angular cut using the rapid RT testing method, which have a non-linear relationship with the radial depth of cut (Eq. 22), therefore, it is not possible to exactly recreate the range of chip loading conditions achieved in the traditional TS testing method across the angular cut using a constant feed rate. This is one of the contributing factors that caused the larger differences in the CFCs calculated between the rapid RT and traditional TS test methods compared to the OS test method, as increased chip load, caused by the increase in the radial depth of cut and feed/rev/tooth, have been shown to reduce the CFCs [5,22].

In addition to the differences in the chip load between the tests, another contributing factor to the differences in the CFCs is the nu-

merical optimisation process that is used by the OS and RT testing methods. Using the traditional TS method, the shearing and ploughing effects were first separated by calculating the gradient and intercept of the F = f(ft) linear regression which provides an extra constraint on the coefficients. However, in the OS and RT methods, the cutting forces were numerically optimised together, which is why the reduction in the shearing coefficients compared to the TS method was accompanied by an increase in the ploughing coefficients. The errors in the predicted cutting forces were not significantly larger because a reduction in the shearing coefficient using the OS and RT methods was always accompanied by an increase in the ploughing coefficients, balancing the force equation. The PSO technique with upper and lower bounds applied to the ploughing coefficients reduced this difference. However, it is not practical to use this method because these bounds require adapting when the material, tool geometry, and cutting conditions are changed and a suitable range cannot be calculated without using the traditional TS testing method. Overall, the particle swarm optimisation method is not necessary to improve the errors in the force models either because the CFCs resulted in a higher residual RMSE.

The RTA and UV force models overall performed consistently compared to each other, the primary factor influencing the model accuracy is the choice of the testing method. The traditional TS testing method performed better than both the OS and RT testing methods, regardless of the choice of force model. The traditional TS-RTA and TS-UV models are the most accurate models, predicting the average cutting forces to within 3 % and 3.3 %, respectively, whilst the OS and rapid RT testing methods had higher errors overall. The rapid RT-RTA and RT-UV models predicted the average F_x , F_y and F_z cutting forces across all the cutting conditions to within 17.79 %, 30.27 %, and 25.21 % error, and 19.7 %, 20.4 %, and 12 % error, respectively. However, neglecting test 1 which had larger experimental variation, the error is significantly reduced, and the RT-RTA and RT-UV models predict the average F_x , F_y and F_z cutting forces to within 3.4 %, 6.2 % error, and 13.4 %, and 4.6 %, 6.35 %, and 5.9 % error, respectively. This demonstrates that the rapid testing method is likely suitable for industrial optimisation applications. Additionally, the good accuracy of the OS method demonstrates that the numerical optimisation CFC calculation approach can be used with cutting force data that has changes in both feed rate and radial engagement; making it useful to calculate CFCs in-process over any complex tool path, provided that the chip load is varied.

This increased error using the OS and RT testing methods is potentially related the different range of chip loads used to identify the CFCs demonstrated previously in Fig. 8a, and the reduced level of information that can be extracted from the testing methods that utilise variable radial engagements to cause changes in chip loading, as highlighted previously in Fig. 8b. The OS testing developed in this study has slightly better accuracy because the chip loads are more consistent with the traditional TS method, and because there was also variation in the feed rates enabling more information to be extracted from the process. The difference in chip loads across the testing methods reasoning is validated by comparing the predicted average forces at the test 3 condition; this is the only chip load consistent across the three testing methods which result in the lowest error in the predicted forces using the CFC identified with the OS and rapid RT testing methods. Indicating that, even though less information is extracted from the process, the rapid RT testing method is still accurate when being used to predict the cutting forces at a chip load that occurred within the CFC identification data. Another potential reason for this increased error in the OS and RT testing method is that these methods lack the prior separation between the shearing and ploughing forces that the traditional TS method benefits from before the CFC calculation.

The UV force model captures the variation of the shearing and ploughing coefficients with the changes in the local helix and rake angle in the bull-nose region of the tool, as well as the variation of the nominal helix angle in the cylindrical part of the tool. In contrast, the RTA models do not capture this change in CFCs with the local geometry, this method

only captures this variation on the ploughing edge length $dS_{k,j}$. However, this is not significantly reducing the accuracy of the RTA models compared to the UV models, although it has potentially resulted in the improvement in the force prediction at the extreme lower and higher chip loads (in tests 1 and 5) using the rapid RT testing method. Therefore, based on these results, the UV force model is recommended when using the rapid testing method and with bull-nose tools with variation in the local cutting-edge geometry.

The disadvantage of the UV force model is that the matrix $[A_k][T_{RI_k}]|T_{IU_{j,k}}|$ used to calculate the shearing forces is non-symmetrical (3×2) , resulting in more equations than coefficients to be solved when calculating the CFCs. These systems have no solution in cases such as this because the equations are inconsistent, therefore, the solution that satisfies the F_x , and F_y forces may not satisfy the F_z force. Due to this, a least squares numerical solution was calculated for all the models that used the UV force model, including the TS-UV model as a secondary optimisation procedure after the fitting of the linear regression, whereas an exact solution to the TS-RTA model was calculated from the gradient and intercepts of the fitted linear regressions. This results in a loss of information when calculating K_{uc} and K_{vc} force coefficients from the experimental F_x , F_y and F_z cutting forces. This effect coupled with only five parameters to be optimised using the UV force model compared to the RTA force models' six, likely contributed to the overall higher RMSE values using the UV force model. Further improvement of the UV force model to incorporate a third oblique force component in the rake face to make the matrix symmetrical is recommended.

The time-domain response of the models is demonstrated at the test 3 cutting condition. The time-domain trends were poorly predicted within the revolution of the tool by all models, even though the average cutting forces were predicted to be within 8 % error across all the models. This disagreement of the predicted forces for complex geometry tools with variable pitch and helix angles in Ti-6Al-4 V has also been observed in the literature by Tunç et al. [10], which predicted the average cutting forces well but underpredicted the peak forces in the time domain response which were also offset from the experimental response.

These deviations are potentially caused by a combination of the fundamental limitations of all average CFC identification techniques, as well as the phenomena in the experimental measurements that were not captured in the model such as run-out and distortion of the measured force data caused by the piezoelectric-based dynamometer [23]. Using the averaged cutting forces to identify the CFCs does not fully utilise the available dataset to capture the variation of the CFCs with uncut chip thickness which has been demonstrated by Rubeo and Schmitz [5], and it removes all information related to individual flute engagements from the data and then expects the model to be able to predict them. The limitation of instantaneous CFC methods is the complexity of capturing the force data that is synchronised with the tool's rotation angle of engagement.

The impact of not capturing the tool geometry correctly on the time-domain force response discrepancies was ruled out because pitch and helix angles of the tool were measured, showing very little deviation from the nominal values used in the models. However, the tool used in the experimental testing had $10~\mu m$ of total run-out which the model did not consider. Although, as the CFCs calculated in this study rely on the averaged calculation method, the run-out does not impact the CFCs, which may be a contributing factor to the inaccuracies in the time-domain response whilst the average forces were predicted well.

Finally, the stiffness of the piezoelectric-based dynamometer and workpiece structure distorts the higher frequency content of the forces, which results in measurement error [23]. This is more critical in high-speed and highly intermittent milling processes [23], whereby this compensation has been shown to significantly reduce the peak forces measured and enables clearer identification of the flute engagement from the force response. This is potentially another contributing factor to the errors in the time-domain response prediction, future work to

characterise the dynamometer dynamics using impulse hammer tests and compensate for these natural frequencies.

6. Conclusions

This work presented a comprehensive study of the merits and limitations of several mechanistic force models and CFC identification testing methods milling operations. The limited range of chip-loads achieved using the RT testing approach that uses a single angular cut was demonstrated and a novel hybrid OS approach was proposed which reduces the impact of this limitation by combining variation in both feed rate and radial engagement. Additionally, a bull-nose tool with variable pitch and helix angles was selected to highlight the advantages of the UV force model compared to the RTA force model, which has not been demonstrated in the literature.

Using the UV force model, and neglecting test 1 which had a higher error due to larger variation in the experimental data, the identified CFCs using the RT testing method predicted the averaged F_x , F_y and F_z cutting forces overall within 4.6 %, 6.3 %, and 5.9 % error, respectively. These errors are slightly higher than those using the traditional TS method which predicted the forces overall to within 1.07 %, 1.9 %, and 3.3 %, respectively. This is potentially caused by the fundamental limitation of the RT method that relies on changes in radial engagements (i. e. changes in start angle for down-milling). This method reduces the total chip load variation in the dataset because it only increases the length of the engagement arc causing a lot of overlap. This limitation of the RT method has not previously been identified in the literature. However, another contribution to the reduced accuracy of the RT method is because chip load ranges were not consistent with the TS testing method. The errors in the predicted average F_x , F_y and F_z cutting forces reduced to 3.3 %, 6.3 %, and 1.7 % at the test 3 cutting condition, when predicting the cutting forces at a chip load consistent across the three testing methods. The non-linear relationship between the chip load and the radial depth of cut means that the exact chip load conditions used to calculate the CFCs using the traditional TS method cannot be recreated in the rapid RT testing when using a constant feed rate. From the authors perspective, this error using the rapid RT method is potentially acceptable for commercial tool path optimisation, and it requires only a singular angular cut to calculate the CFCs, which is the key benefit for commercial implementation.

The OS testing method demonstrates that the optimisation approach used by the rapid RT testing method can also be used to calculate the CFCs when both the radial depth of cut and the feed rate are varied. This testing method, coupled with the UV force model and neglecting test 1, predicted the averaged F_x , F_y and F_z cutting forces overall to within 7.1 %, 4.3 %, and 3.8 % error, respectively. This is marginally better than the RT method for the F_y and F_z force components. This is likely because the variation in feed rate along with the radial engagement increased the variation of chip loading in the data, it partly reduced the large overlap in chip load that is found by varying radial engagement alone. The OS method demonstrates that the optimisation approach used in the rapid testing method can also be successfully implemented to calculate the CFCs in-process over a complex tool path, provided the chip load is varied. The industrial implication of this is that CFCs could potentially be calculated whilst machining real-world components.

The CFCs calculated using the rapid RT and OS methods are different from those using the traditional TS method because a numerical optimisation method is utilised that lacks the prior separation of the shearing and ploughing force components of the traditional TS testing method. However, this did not significantly impact the predicted cutting forces because the reduction in the shearing coefficients was compensated by the increase in the ploughing coefficients, resulting in similarly predicted cutting forces.

The more recently developed UV force model was also compared with the RTA approach, and it was shown that they performed similarly.

The primary factor impacting the model accuracy was found to be the choice of the testing method. However, the UV method performed better than the RTA force model with the RT method at the upper and lower feed rates in this study, whereas they performed consistently when using the traditional TS identification method.

Further improvement of the UV force model is recommended to include a third force component in the rake face to prevent an overdetermined system of equations when calculating the shearing force coefficients. The UV model currently must be implemented with a numerical optimisation procedure, regardless of the testing method, including the traditional TS method which requires a secondary optimisation procedure after the fitting of the linear regression to calculate the CFCs. This, coupled with one less coefficient to optimise compared the RTA force model, results in the UV models having higher residual root-mean-squared error of fit with the experimental data than the RTA models. Regardless of these limitations, the UV force model generally performed better than the RTA approach and it was able to capture the variation of the local helix in the bull-nose region of the tool used in this study.

The time-domain force prediction predicted peaks in force that were offset from the experimentally measured response, which was consistent with the finding in the literature for complex variable pitch and helix tools. The reason for this discrepancy is potentially because the CFC identification methods used in this study were all based on the averaged cutting forces approach which does not fully utilise the available dataset to capture the variation of the CFCs with uncut chip thickness. Along with limitations in the model, such as not capturing the tool run-out. Further work is necessary to implement the effect of tool run-out and to filter the natural frequencies of the dynamometer from the measured force data to further isolate the effect of CFC identification method and force model.

CRediT authorship contribution statement

David Curtis: Writing – review & editing, Supervision, Resources, Funding acquisition. Zekai Murat Kilic: Writing – review & editing, Supervision, Methodology, Conceptualization. Peace Onawumi: Investigation, Data curation. Javier Dominguez-Caballero: Methodology, Investigation, Data curation. Sabino Ayvar-Soberanis: Writing – review & editing, Supervision, Project administration, Methodology, Conceptualization. Joshua Priest: Writing – original draft, Visualization, Validation, Software, Methodology, Formal analysis, Conceptualization.

Declaration of Competing Interest

The authors declare that they have no known competing financial interests or personal relationships that could have appeared to influence the work reported in this paper.

Acknowledgements

This research was funded by the High Value Manufacturing Catapult.

References

- Altintas Y, Lee P. Mechanics and dynamics of ball end milling. J Manuf Sci Eng Trans ASME 1998;vol. 120(4):684–92. https://doi.org/10.1115/1.2830207.
- [2] Gradišek J, Kalveram M, Weinert K. Mechanistic identification of specific force coefficients for a general end mill. Int J Mach Tools Manuf 2004;vol. 44(4):401–14. https://doi.org/10.1016/j.ijmachtools.2003.10.001.
- [3] Budak E, Altintas Y, Armarego EJA. Prediction of milling force coefficients from orthogonal cutting data. J Manuf Sci Eng 1996;vol. 118(2):216–24.
- [4] Engin S, Altintas Y. Mechanics and dynamics of general milling cutters. Part II: inserted cutters. Int J Mach Tools Manuf 2001;vol. 41:2213–31.
- [5] Rubeo MA, Schmitz TL. Mechanistic force model coefficients: a comparison of linear regression and nonlinear optimization. Precis Eng 2016;vol. 45:311–21. https://doi.org/10.1016/j.precisioneng.2016.03.008.
- [6] Utsumi K, Shichiri S, Sasahara H. Determining the effect of tool posture on cutting force in a turn milling process using an analytical prediction model. Int J Mach Tools Manuf 2020;vol. 150. https://doi.org/10.1016/j.ijmachtools.2019.103511.
- [7] Kang G, Kim J, Choi Y, Lee DY. In-process identification of the cutting force coefficients in milling based on a virtual machining model. Int J Precision Eng Manuf 2022;vol. 23(8):839–51. https://doi.org/10.1007/s12541-022-00677-4.
- [8] Engin S, Altintas Y. Generalized modeling of milling mechanics and dynamics: Part I-helical end mills'. in ASME 1999 Int Mech Eng Congress and Exposition, Vanocuver. B C 1999:14–9.
- [9] A. Çomak O. Ozkirimli E. Budak Modeling and simulation based design of variable pitch and variable helix milling tools for increased chatter stability 7th International Conference and Exhibition on Design and Production of Machines and Dies/Molds. Antalva 2013.
- [10] Taner TL, Ömer Ö, Erhan B. Generalized cutting force model in multi-axis milling using a new engagement boundary determination approach. Int J Adv Manuf Technol 2015:vol. 77(1–4):341–55. https://doi.org/10.1007/s00170-014-6453-8.
- [11] Niu J, Ding Y, Zhu LM, Ding H. Mechanics and multi-regenerative stability of variable pitch and variable helix milling tools considering runout. Int J Mach Tools Manuf 2017;vol. 123:129–45. https://doi.org/10.1016/j.ijmachtools.2017.08.006.
- [12] Gao G, Wu B, Zhang D, Luo M. Mechanistic identification of cutting force coefficients in bull-nose milling process. Chinese J Aeronautics 2013;vol. 26(3): 823–30. https://doi.org/10.1016/j.cja.2013.04.007.
- [13] Okafor AC, Sultan AA. Development of a mechanistic cutting force model for wavy-edge bull-nose helical end-milling of inconel 718 under emulsion cooling strategy. Applied Mathematical 2016;vol. 40(4):2637–60. https://doi.org/10.1016/j.apm.2015.09.040.
- [14] Kaymakci M, Kilic ZM, Altintas Y. Unified cutting force model for turning, boring, drilling and milling operations. Int J Mach Tools Manuf Mar. 2012;vol. 54–55: 34–45. https://doi.org/10.1016/j.ijmachtools.2011.12.008.
- [15] Armarego E.JA. Unified-generalized mechanics of cutting approach a step towards a house of predictive performance models for machining operations. Mach Sci Technol 2000;vol. 4(3):319–62. https://doi.org/10.1080/10940340008945715.
- [16] Lorain R, Kilic ZM, Valiorgue F, Rech J, Altintas Y. Identification of dynamic coefficient matrix for drilling process simulations from measured tool geometry, axial force and torque. CIRP J Manuf Sci Technol 2024;vol. 52:159–74. https://doi. org/10.1016/J.CIRPJ.2024.05.018.
- [17] Kilic ZM, Altintas Y. Generalized mechanics and dynamics of metal cutting operations for unified simulations. Int J Mach Tools Manuf 2016;vol. 104:1–13. https://doi.org/10.1016/j.ijmachtools.2016.01.006.
- [18] Huang CY, Wang JJJ. Mechanistic modeling of process damping in peripheral milling. J Manuf Sci Eng 2007;vol. 129(1):12–20. https://doi.org/10.1115/ 1.2335857.
- [19] Liu YP, Kilic ZM, Altintas Y. Monitoring of in-process force coefficients and tool wear. CIRP J Manuf Sci Technol 2022;vol. 38:105–19. https://doi.org/10.1016/j. cirpj.2022.04.009.
- [20] Mammadov B, Mohammadi Y, Farahani ND, Altintas Y. A unified FFT-based mechanistic force coefficient identification model for isotropic and anisotropic materials. CIRP J Manuf Sci Technol 2024;vol. 49:216–29. https://doi.org/ 10.1016/J.CIRPJ.2024.01.009.
- [21] G.V. Stabler. The fundamental geometry of cutting tools in Proceedings of the Institution of Mechanical Engineers 1951 14 26 doi: 10.1243/PIME_PROC_1951_ 165 008 02
- [22] Grossi N, Sallese L, Scippa A, Campatelli G. Speed-varying cutting force coefficient identification in milling. Precis Eng 2015;vol. 42:321–34. https://doi.org/ 10.1016/j.precisioneng.2015.04.006.
- [23] Jullien-Corrigan A, Ahmadi K. Measurement of high-frequency milling forces using piezoelectric dynamometers with dynamic compensation. Precis Eng 2020;vol. 66: 1–9. https://doi.org/10.1016/j.precisioneng.2020.07.001.